Journal of Materials Chemistry A

ROYAL SOCIETY OF CHEMISTRY

PAPER

View Article Online
View Journal | View Issue

Cite this: J. Mater. Chem. A, 2025, 13, 22931

Phase equilibrium during the synthesis of $LiNi_{0.46}Mn_{1.54}O_4$: comprehensive X-ray & neutron powder diffraction study†

Ilia Tertov,[abc] François Fauth,[d] Emmanuelle Suard,[a] Thomas Hansen,[a] François Weill,[bf] Pierre-Etienne Cabelguen,[e] Christian Masquelier *[cfg] and Laurence Croguennec *[bf]

A combination of synchrotron X-ray powder diffraction (SXRPD) and neutron powder diffraction (NPD) is used to investigate phase equilibrium during the synthesis of $LiNi_{0.46}Mn_{1.54}O_4$ (LNMO) powders from a reagent mixture. A Li-deficient disordered LNMO begins to form at $T \approx 460$ °C and as the temperature increases, oxygen release triggers the formation of impurity phases. Advanced structural characterization of quenched LNMO samples, along with *in situ* SXRPD experiments, reveals that a layered oxide impurity crystallizes between 700 °C and 900 °C. At temperatures of 900 °C and above, this impurity phase transforms into a rock-salt type one, while a Li-rich layered oxide impurity also emerges. This leads to the coexistence of three phases at $T \geq 900$ °C: LNMO spinel, rock salt, and Li-rich layered oxide. These transformations affect significantly the composition of the targeted LNMO spinel phase, which highlights the challenges in achieving phase purity with the desired stoichiometry in this complex system. The findings provide valuable insights for optimizing the LNMO synthesis so as to prepare high-performance positive electrode materials.

Received 23rd February 2025
Accepted 3rd June 2025

DOI: 10.1039/d5ta01514f

rsc.li/materials-a

Introduction

$LiNi_{0.5}Mn_{1.5}O_4$ (LNMO) is recognized as a highly promising spinel-type positive electrode material for Li-ion batteries (LIBs). Its high operating voltage of 4.8 V *versus* Li^+/Li, driven by the $Ni^{4+}/Ni^{3+}/Ni^{2+}$ redox couples, offers a significant energy density, which is essential for developing next-generation LIBs.[1]

LNMO crystallizes in the spinel structural type with different degrees of Mn/Ni ordering. In the fully disordered LNMO phase ($Fd\bar{3}m$ S.G.) Li^+ cations occupy the tetrahedral 8*c* sites while Ni and Mn cations are randomly distributed on the 16*d* octahedral sites. In contrast, in the ideally ordered LNMO phase ($P4_332$ S.G.), Li^+ cations are located at the tetrahedral 8*a* sites, and Ni and Mn cations occupy the 4*b* and the 12*d* octahedral sites, respectively. Disordered LNMO can be prepared by annealing at temperatures above 730 °C under air, while lower temperatures lead to the formation of the ordered LNMO.[2–4] On top of that, oxygen release starts at $T \geq 700$ °C under air and at $T \geq 720$ °C under oxygen, leading to Ni loss from the LNMO spinel phase as a consequence of the formation of a Ni-enriched rock-salt-type impurity.[5]

The most commonly used route for synthesizing LNMO powders is the solid-state method, which commonly consists of two stages.[1] In the first stage, the reagent mixture undergoes high-temperature annealing at $T = 900$ °C, leading to significant oxygen loss and to the formation of disordered LNMO along with a large amount of rock salt impurity phase. In the second stage, the powder is annealed at a lower temperature, typically 600–700 °C, which promotes oxygen intake, reduces the amount of impurity phase, and facilitates the formation of ordered LNMO.[2,6]

[a]Institut Laue-Langevin, 38042, Grenoble, France
[b]Univ. Bordeaux, CNRS, Bordeaux INP, ICMCB UMR 5026, F-33600, Pessac, France. E-mail: laurence.croguennec@icmcb.cnrs.fr
[c]Laboratoire de Réactivité et de Chimie des Solides, Université de Picardie Jules Verne, UMR CNRS 7314, F-80039, Amiens Cedex 1, France. E-mail: christian.masquelier@u-picardie.fr
[d]CELLS-ALBA Synchrotron, Cerdanyola del Vallès, E-08290 Barcelona, Spain
[e]Umicore, 31 rue du marais, Brussels BE-1000, Belgium
[f]RS2E, Réseau sur le stockage électrochimique de l'énergie, FR CNRS 3459, F-80039, Amiens Cedex 1, France
[g]Institut Universitaire de France, 103 boulevard Saint-Michel, 75005 Paris, France

† Electronic supplementary information (ESI) available: Rietveld plot after the refinement of the XRPD pattern for the sample prepared by firing of $Ni_{0.23}Mn_{0.77}(OH)_2$. TG data obtained under air for the mixture of Li_2CO_3 and $Ni_{0.23}Mn_{0.77}(OH)_2$. Rietveld plots after refinements of SXRPD and NPD patterns of the mixture of Li_2CO_3 and $Ni_{0.23}Mn_{0.77}(OH)_2$ collected at 650 °C during *in situ* experiments. *In situ* NPD data for the mixture of Li_2CO_3 and $Ni_{0.23}Mn_{0.77}(OH)_2$. The detailed description of the Rietveld refinement procedures. The *in situ* SXRPD patterns of the LNMO sample at given temperatures, collected under air and oxygen atmospheres. Experimental points, as well as calculated and difference plots after the Rietveld refinement of SXRPD and NPD patterns for the pristine and quenched LNMO samples. Comparison of Raman spectra of the q900 °C sample and $LiNi_{0.5}Mn_{0.3}Co_{0.2}O_2$. Insights into the structural relationship between the layered oxide $LiMO_2$ and the rock salt $Li_{1-x}M_xO$. See DOI: https://doi.org/10.1039/d5ta01514f

As most LNMO samples described in the literature contain both LNMO spinel and rock salt impurity phases, it is important to distinguish between the composition of the LNMO phase and the overall composition of the samples. According to Cabana *et al.*,[5] the rock salt impurity phase is richer in nickel, with a Mn/Ni ratio of 2 : 1, compared to 3 : 1 in the LNMO $LiNi_{0.5}Mn_{1.5}O_4$ spinel phase. This indicates that the formation of the impurity phase alters the composition of the LNMO spinel phase, enriching it with Mn according to $LiNi_{0.5-x}Mn_{1.5+x}O_4$.

In several studies,[2,5–8] it was shown that disordered LNMO exhibits superior electrochemical performance at high charge/discharge rates and better cycling stability than ordered LNMO. However, the reasons for this enhanced performance in disordered LNMO are more complex than simply the effect of Ni and Mn disorder. In a previous work,[9] we demonstrated that the chemical composition of the LNMO spinel phase is a more critical factor in determining the material's performance than the degree of Mn/Ni ordering. Materials with a slight excess of Mn in the LNMO spinel phase showed the most favorable performance at high C-rates and better cycling stability. Therefore, understanding the evolution of the LNMO spinel phase composition is essential for synthesizing the best-performing materials.

Although the LNMO system may seem well-studied, various inconsistencies still exist in the literature. Recently, Stüble *et al.*[10] and Chen *et al.*[11] demonstrated that Li loss from the LNMO phase occurs at $T > 700$ °C, leading to the occupancy of Li (8*a*) sites by transition metal cations. This was shown using *in situ* laboratory X-ray powder diffraction (XRPD)[9] and *in situ* neutron powder diffraction (NPD).[10] Chen *et al.*[11] also suggested that both Ni and Mn atoms can occupy Li sites within the LNMO structure as *in situ* NPD experiment in the temperature range of 700–800 °C revealed that the atomic density at the Li sites changed non-monotonically: it increased between 700 °C and 750 °C, but began to decrease above 750 °C. Considering that the coherent scattering lengths (b_{coh}) of Li and Mn have negative values of −1.9 fm and −3.7 fm respectively, while Ni has a positive b_{coh} of 10.3 fm, they hypothesized that Ni atoms initially occupy the Li sites, but as the temperature increases, Mn atoms start to occupy these sites also. However, since both Li and Mn have negative b_{coh} values, this non-monotonic change in atomic density at the Li sites might also be related to the fluctuating amount of Li rather than the presence of Mn atoms. Combining NPD and XRPD would enable a more detailed study of these variations in the chemical composition of the LNMO phase. Due to the similarity in the scattering factors of Mn and Ni, XRPD allows for distinguishing between Li and transition metal (Ni and Mn) atoms.

Many discrepancies are also related to the type of impurity phase observed. For example, the *in situ* temperature-controlled XRPD study of LNMO conducted by Stüble *et al.*[10] revealed the formation of a rock salt impurity phase, only, under an air atmosphere. Similarly, Pasero *et al.*[3] and Cabana *et al.*,[5] who investigated a series of LNMO samples quenched from temperatures in the range of 800–1000 °C under air, also reported the formation of only the rock salt impurity phase. However, Chen *et al.*[11] using *in situ* temperature-controlled NPD, surprisingly observed the formation of a layered oxide impurity under an Ar atmosphere, while only the rock salt impurity was detected under air. The reasons for the formation of the layered oxide impurity in an Ar atmosphere and the rock salt one in air remain unclear, as both share similar chemical formula of $Li_{1-x}M_{1+x}O_2$. It is possible that the layered oxide phase also forms in air, but due to the limited resolution of laboratory XRPD and NPD, as well as the similarity between the diffraction patterns of layered oxide and rock salt phases, it has not been detected.

In this fundamental study, we investigated for the first time the formation of the LNMO spinel phase (from the reagent mixture) using *in situ* temperature-controlled synchrotron XRPD (SXRPD) and NPD techniques. Since our previous work demonstrated that a slight excess of Mn positively impacts the electrochemical performance,[9] we decided to investigate a Mn-rich LNMO sample with a global Mn/Ni ratio of 77/23. The use of SXRPD also allowed us to gain a more detailed understanding of the phase equilibrium and structural transformations occurring in the LNMO spinel and impurity phases during synthesis. Additionally, we extensively employed a quenching procedure so as to thoroughly examine changes in the chemical composition and cation distribution of the LNMO spinel phase through SXRPD and NPD.

Experimental

Synthesis

A pristine Mn-rich mixed nickel–manganese hydroxide sample (with Mn/Ni = 77/23, $Ni_{0.23}Mn_{0.77}(OH)_2$ from Umicore, Belgium) was used hereafter as precursor for *in situ* SXRPD experiments and for the preparation of quenched samples. It was fired as a 1 : 4 molar mixture with Li_2CO_3 in an alumina crucible in a muffle furnace under a synthetic air and atmosphere (mixture of dry N_2 and O_2) with the following the heating and cooling programs: heating at a rate of 5 °C min^{-1} up to 500 °C followed by 1 °C min^{-1} up to 1050 °C and kept for 12 hours at 1050 °C. Subsequently, the powder was cooled down to room temperature within 12 hours to yield a so-called pristine LNMO sample. The quenched samples were prepared by heating the pristine LNMO sample in a tube furnace under synthetic air, using an alumina boat, with the heating rate of 1 °C min^{-1} followed by annealing for 12 hours at 750 °C, 800 °C, 850 °C, 900 °C or 950 °C. The resulting powders were quickly taken out of the furnace for rapid cooling (quenching) under air. Another series of quenched samples was prepared at 600 °C, 650 °C and 700 °C directly from the mixture of Li_2CO_3 and $Ni_{0.23}Mn_{0.77}(OH)_2$ without annealing. Additionally, one sample was kept for 2 hours (instead of 12 hours) at 650 °C before being quenched as already described.

Materials characterization

In situ temperature-controlled SXRPD experiments were performed using the BL04-MSPD beamline (ALBA, Spain)[12] with wavelengths of 0.6206 Å and 0.7092 Å in Debye–Scherrer geometry from samples placed in 0.7 mm diameter quartz

capillaries. The sample was either the 1 : 4 mixture of Li_2CO_3 and $Ni_{0.23}Mn_{0.77}(OH)_2$ or the pristine Mn-rich LNMO sample mentioned above. For the experiment under oxygen, the quartz capillary containing the powder was sealed under oxygen atmosphere. For the experiments under air, one-end-open capillaries were used. The samples were heated with a hot air blower (FMB Oxford) positioned above the capillary with the heating rates of 5 °C min^{-1} up to 500 °C followed by 1 °C min^{-1} up to 900 °C. The temperature calibration was performed beforehand by measurement of the hot gas temperature at the sample position with an independent thermocouple and further cross-checked by collecting the data around phase transition temperatures for Na_2CO_3 ($C2/m \rightarrow P6_3/mmc$ S.G. at 483 °C, melting at 851 °C), SiO_2 (α- to β-quartz at 573 °C), NaCl (melting at 801 °C).

An *in situ* temperature-controlled NPD experiment was performed at the D20 High-Intensity 2-axis Diffractometer (Institut Laue-Langevin, Grenoble, France) with a wavelength of 1.54 Å in Debye–Scherrer geometry. Approximately 5 g of the 1 : 4 molar mixture of Li_2CO_3 and $Ni_{0.23}Mn_{0.77}(OH)_2$ were placed in the middle of the two-end-open quartz tube with outer diameter of 12 mm and inner diameter of 8 mm. To ensure a good contact with the gas atmosphere, the flow of synthetic air was circulating through the sample. The sample was heated in the D20's dedicated furnace equipped with a vanadium heating element, the heating rates being of 5 °C min^{-1} up to 500 °C and then of 1 °C min^{-1} up to 800 °C. Due to technical limitations related to the mechanical and chemical stability of the vanadium heating element and the quartz tube, the maximum temperature in the *in situ* NPD experiment was limited to 800 °C.

The SXRPD patterns of the pristine and quenched LNMO samples, obtained *ex situ* as described above, were collected at room temperature at the BL04-MSPD beamline (ALBA, Spain), using the same geometry, in sealed 0.7 mm diameter borosilicate glass capillaries. The NPD patterns were collected at room temperature at the D2B High-Resolution Diffractometer (Institut Laue-Langevin, Grenoble, France) with a wavelength of 1.59 Å in Debye–Scherrer geometry. The samples were loaded in vanadium cylindrical holders of 8 mm diameter.

The instrumental profile function of BL-04 MSPD SXPRD diffractometer and D2B High-Resolution NPD diffractometer were determined using $Na_2Ca_3Al_2F_{14}$ as a standard sample. Treatment of diffraction data and Rietveld refinements were performed using the Jana2006 (ref. 13) and the FullProf suite software[14] packages. Additional Lorentzian broadening observed for superstructure reflections of the ordered LNMO ($P4_332$ S.G.), present as signature of small antiphase domains, was refined with FullProf using size model #-2.

Raman spectra were obtained with a confocal LabRAM HR Evolution micro-spectrometer (Horiba) using a 560 nm argon gas laser source and a 600 gr mm^{-1} grating. Each spectrum was recorded over the range of 100 to 800 cm^{-1} using a 10.6 mm focal length lens, with a 10-seconds acquisition time and 40 accumulations. To access a reproducibility, Raman spectra were collected at different particles within the samples.

Transmission electron microscopy (TEM) images and electron diffraction (ED) patterns were collected using a JEOL 2000FX microscope, both equipped with double-tilt specimen holders and operated at an accelerating voltage of 200 kV. The powder sample was ground in ethanol, and a droplet of the resulting suspension was deposited onto a lacey carbon grid. The particles selected for study were as isolated and as thin as possible.

Thermogravimetric analyses were performed on a TGA Setaram TAG 2400. The experiments were carried out under air at a heating rate of 1 °C min^{-1}.

Results and discussion

Formation of the LNMO spinel phase from the reagent mixture

Moderate temperature range, from RT to 700 °C. On the SXRPD pattern collected at RT for the mixture of Li_2CO_3 and $Ni_{0.23}Mn_{0.77}(OH)_2$ (Fig. 1a, bottom), sharp and low-intensity reflections can be assigned to Li_2CO_3 ($C2/c$ space group, ICSD # 66942). The most intense reflection at $2\theta \approx 7.6°$ corresponds to the $Ni_{0.23}Mn_{0.77}(OH)_2$ layered hydroxide.

During heating, the lattice parameters of Li_2CO_3 and $Ni_{0.23}Mn_{0.77}(OH)_2$ increase (thermal expansion). At $T \approx 300$ °C, a high-intensity reflection at $2\theta \approx 14.5°$ appears with the disappearance of the most intense reflection of the $Ni_{0.23}Mn_{0.77}(OH)_2$ hydroxide at $2\theta \approx 7.6°$. In other words, the dehydration of the $Ni_{0.23}Mn_{0.77}(OH)_2$ hydroxide occurs through the formation of a new phase.

Thanks to additional experiments (described in ESI and in Fig. S1†), this new phase was identified as ilmenite-type $Ni_xMn_{2-x}O_3$ (Fig. 1a, middle). At $T > 300$ °C the sample consists of three phases: Li_2CO_3, $Ni_xMn_{2-x}O_3$ as a main phase and $Ni_yMn_{1-y}O(OH)$ as an impurity. Upon further heating, at $T \approx 460$ °C, new reflections start to appear together with the disappearance of the reflections of Li_2CO_3, $Ni_xMn_{2-x}O_3$ and $Ni_yMn_{1-y}O(OH)$. At $T = 700$ °C, all the reflections on the SXRPD pattern can be indexed using a face-centered cubic cell described within the $Fd\bar{3}m$ space group (S.G.) with $a = 8.2377(2)$ Å, corresponding to the LNMO phase (Fig. 1a, top).

A similar reaction pathway is observed during the *in situ* temperature-controlled NPD experiment (Fig. 1b). The dehydration of $Ni_{0.23}Mn_{0.77}(OH)_2$ with the formation of ilmenite-based $Ni_xMn_{2-x}O_3$ oxide and $Ni_yMn_{1-y}O(OH)$ oxyhydroxide also starts at $T \approx 300$ °C and is followed by the appearance of LNMO reflections at $T \approx 460$ °C. It is important to mention that all the reflections on the NPD pattern at 700 °C can be indexed in the $Fd\bar{3}m$ S.G. ($a = 8.2378(3)$ Å), as for the SXRPD pattern at $T = 700$ °C. Thus, it shows that the disordered LNMO phase is forming initially during the synthesis.

The observed reaction pathway is also in good agreement with thermogravimetric analysis (TGA) data (Fig. S2a†), collected under air with heating rates similar to those used during the *in situ* SXRPD and NPD experiments. Severe weight loss starts at $T \approx 300$ °C and corresponds to dehydration of $Ni_{0.23}Mn_{0.77}(OH)_2$. The weight loss ends at $T \approx 540$ °C, which corresponds to the full disappearance of the reflections of Li_2CO_3, $Ni_xMn_{2-x}O_3$ and $Ni_yMn_{1-y}O(OH)$ in *in situ* collected SXRPD (Fig. 1a) and NPD (Fig. 1b) patterns.

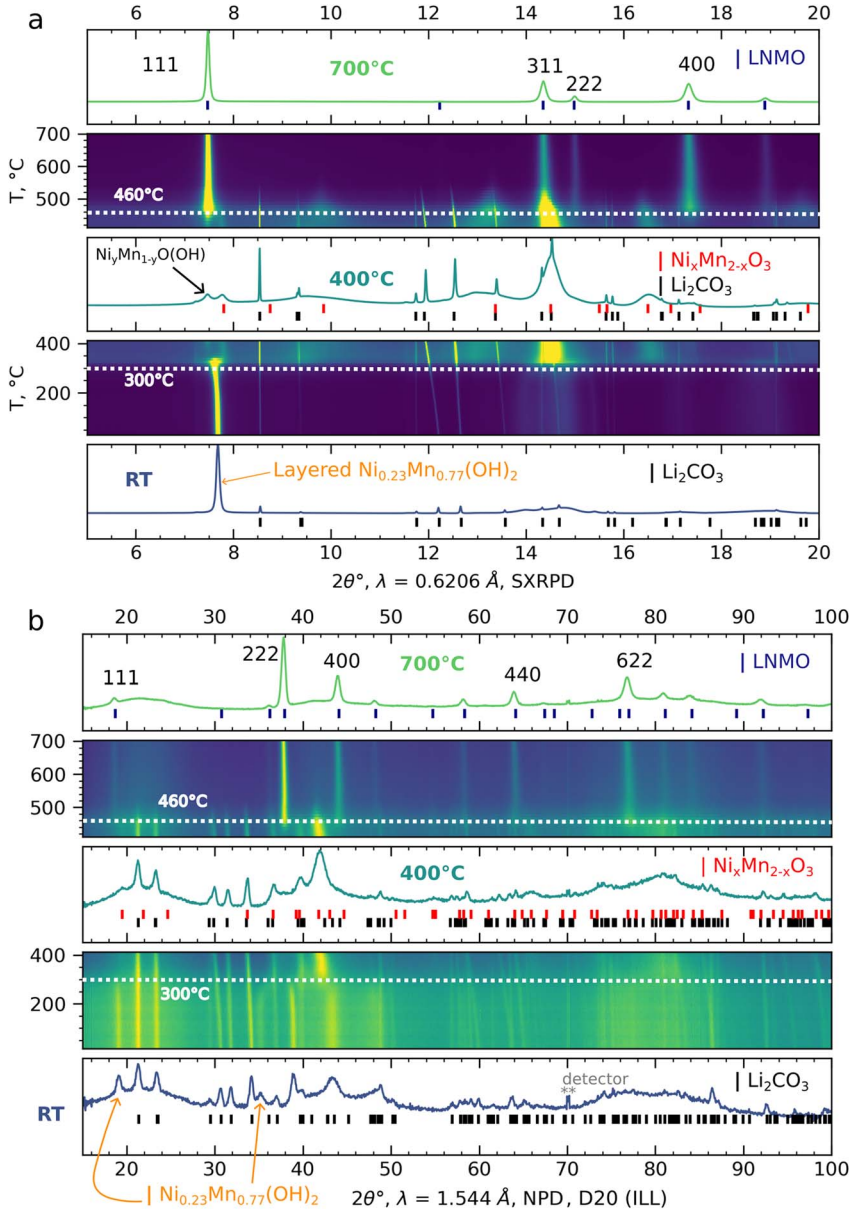

Fig. 1 *In situ* T-controlled SXRPD (a) and NPD data (b) of the mixture of Li_2CO_3 and $Ni_{0.23}Mn_{0.77}(OH)_2$ collected at room temperature (bottom), at 400 °C (middle) and at 700 °C (top). Contour plots represent the evolution of SXRPD patterns from room temperature to 400 °C, and from 400 °C to 700 °C.

It should be noted, that the observed weight loss of ≈16% is in a good accordance with the expected weight loss of 15.7% for the overall chemical reaction (eqn (1)) which describes the formation of the LNMO phase with the chemical composition of $LiNi_{0.46}Mn_{1.54}O_4$. According to *in situ* SXRPD and NPD data, it can be suggested that the chemical reaction is completed already at $T \geq 600$ °C, at which only the disordered LNMO phase is observed.

$$2Li_2CO_3 + 8Ni_{0.23}Mn_{0.77}(OH)_2 + 3O_2 = 4LiNi_{0.46}Mn_{1.54}O_4 + 2CO_2\uparrow + 8H_2O \quad (1)$$

To evaluate the chemical composition of the LNMO spinel phase formed during the *in situ* experiments, Rietveld refinements from the SXRPD and NPD patterns collected at 650 °C were carried out (detailed description of the Rietveld refinement procedure in ESI†). In the case of SXRPD, the difference Fourier analysis revealed an excess of electron density at the 8*a* sites (Li sites) and therefore Ni atoms were placed at the Li sites, for the Rietveld refinement which converged to 4.73(8)% Ni in the 8*a* sites. Experimental points, as well as the calculated and difference plots after the Rietveld refinement of the SXRPD pattern collected *in situ* at 650 °C can be found in Fig. S2b.†

It is noteworthy that based on SXRPD data, the similar scattering factors of Ni and Mn prevented us from determining whether Ni, Mn, or both at the same time occupy the Li sites.

However, due to the opposite signs of coherent scattering lengths b_{coh} of Ni (10.3 fm) and Mn (−3.7 fm), NPD data can indicate which elements predominantly occupy the Li sites (b_{coh} = −1.9 fm). The presence of Ni atoms at the Li sites increases atomic density, whereas the presence of Mn atoms decreases it. The difference Fourier synthesis clearly showed an increase in atomic density at the Li sites in this case, indicating that the transition metal atoms mainly occupying the Li sites are Ni atoms. Additionally, the occupancy factors of Ni and Mn at the 16*d* sites were refined with the constraint Ni + Mn = 100%. As a result, the following chemical formula can be written for the LNMO spinel phase formed *in situ* at 650 °C during the NPD experiment: $(Li_{0.93(2)}Ni_{0.07(2)})_{8a}(Ni_{0.424(3)}Mn_{1.576(3)})_{16d}O_4$. The corresponding experimental points, as well as the calculated and difference plots can be found in Fig. S2c.†

According to the results of the Rietveld refinement of the SXRPD and NPD patterns collected at 650 °C, the composition of the LNMO spinel phase does not match the targeted composition of $LiNi_{0.46}Mn_{1.54}O_4$, meaning that the chemical reaction between Li_2CO_3, $Ni_xMn_{2-x}O_3$ and $Ni_yMn_{1-y}O(OH)$ is not yet fully completed at 650 °C. Since only the LNMO spinel phase is observed in the SXRPD and NPD patterns, it can be inferred that amorphous phases, which cannot be detected, may still be present in the sample at this temperature. Our results also suggest that the crystal structure of the initially formed LNMO spinel phase is disordered, as no superstructure reflections of the ordered LNMO phase are observed on the NPD patterns.

To investigate the formation of the LNMO phase at the early stages of the synthesis, we prepared a series of samples quenched under synthetic air at 600 °C, 650 °C and 700 °C (noted as q600 °C, q650 °C and q700 °C) using the same mixture of Li_2CO_3 and $Ni_{0.23}Mn_{0.77}(OH)_2$, and heating rates as for the *in situ* experiments. Additionally, one sample was kept for 2 h at 650 °C before being quenched (noted as q650 °C 2 h). The resulting NPD and SXRPD patterns collected at RT after the quenching can be found in Fig. 2a and b. Those of the q600 °C, q650 °C and q700 °C samples can be indexed in the $Fd\bar{3}m$ S.G., whereas in the NPD pattern of the q650 °C 2 h sample additional low-intense and broad reflections are present, which can be indexed in the $P4_332$ S.G. In other words, the superstructure reflections of the ordered LNMO phase are already observed. According to Casas-Cabanas *et al.*,[15] Kim *et al.*[2] and Oney *et al.*[16] their broadening can be attributed to the formation of small domains of ordered LNMO at the particle level.

The detailed description of the combined Rietveld refinement of SXRPD and NPD patterns of the q600 °C, q650 °C, q700 °C and q650 °C samples can be found in ESI.† The results are compared in Table 1. For an illustration of the quality of the refinement, experimental points, as well as calculated and difference plots obtained for the q650 °C 2 h sample are given in Fig. 2c and d.

The results presented in Table 1 align with the data from *in situ* NPD and SXRPD experiments. At the early stages of the synthesis (≈600 °C), a Li-deficient LNMO spinel phase forms, with Ni atoms occupying the Li sites. As the temperature increases and the chemical reaction progresses, the Li deficiency in the LNMO crystal structure decreases, bringing its composition closer to the $LiNi_{0.46}Mn_{1.54}O_4$ target composition, also achieved after annealing for 2 hours at 650 °C. Furthermore, in these conditions, the ordering of Mn and Ni in the octahedral sites begins, leading to the formation of small ordered domains, approximately 7 nm in size. In other words, increasing the temperature and/or annealing time moves the system closer to its equilibrium state and to the targeted composition.

High-temperature range, from 700 °C to 900 °C. Selected SXRPD patterns collected at given temperatures during *in situ* experiment can be found in Fig. 3a. With an increase of temperature, reflections of impurity phases appear. Surprisingly, on the pattern collected at 850 °C, the impurity reflection at $2\theta \approx 7.3°$ closed to the (111) reflection of LNMO cannot be described by the face-centered cubic unit cell of the rock salt impurity.

Moreover, the broad signature at $2\theta \approx 14.7°$, next to the (222) reflection of LNMO, is in fact due to two reflections. In this 2θ range, only the (111) reflection is theoretically present for the rock salt impurity, which implies that this "impurity" possesses lower symmetry than the cubic rock salt. All these reflections can be indeed indexed in a rhombohedral cell described within the $R\bar{3}m$ S.G. with the following lattice parameters: $a = 2.953(5)$ Å, $c = 14.53(1)$ Å ($c/a = 4.920(2)$). As a conclusion, a layered oxide impurity initially forms during the synthesis and then upon heating, the reflections (006) and (012) of the layered oxide impurity merge into a single reflection with much higher intensity. In fact, the reflections of the impurity phase identified in the pattern collected at 903 °C can be indexed in the $Fm\bar{3}m$ S.G. with $a = 4.198(1)$ Å, showing a transformation from the rhombohedral layered structure to the cubic rock salt structure (Fig. 3b).

Another important structural parameter to be discussed relates to the possible occupation of Li sites by transition metals and we note that the intensity of the (220) reflection ($I_{220} \approx f_{8a(Li)}^2$) of the LNMO phase indeed dramatically increases with temperature (Fig. 3a) as a clear signature of the partial occupation of the 8*a* sites by transition metal atoms (Ni and/or Mn). As discussed above, for SXRPD, similar scattering factors of Ni and Mn do not allow to properly distinguish them. For the Rietveld refinements of the structures from patterns collected *in situ* at 850 °C and 900 °C, a two-phase model was employed (ESI†). Experimental points, as well as calculated and difference plots are compared for both temperatures in Fig. 4. At 850 °C, the refined amount of Ni at the Li sites in the LNMO spinel phase was found to be 9.1(1)%, and the weight fraction of LNMO 80.5(2)%. At 900 °C, the amount of Ni at the Li sites increased to 16.0(1)%, and the weight fraction of LNMO decreased to 67.0(3)%. Unfortunately, due to technical restrictions, the *in situ* temperature-controlled NPD experiment was conducted only up to 800 °C (Fig. S3a†). Additionally, the relatively poor crystallinity of the formed LNMO phase and the significantly broader reflections in general, caused by the broader instrumental function of the D20 diffractometer, prevented us from clear distinguishing between layered oxide impurity and rock salt impurity. However, the Rietveld

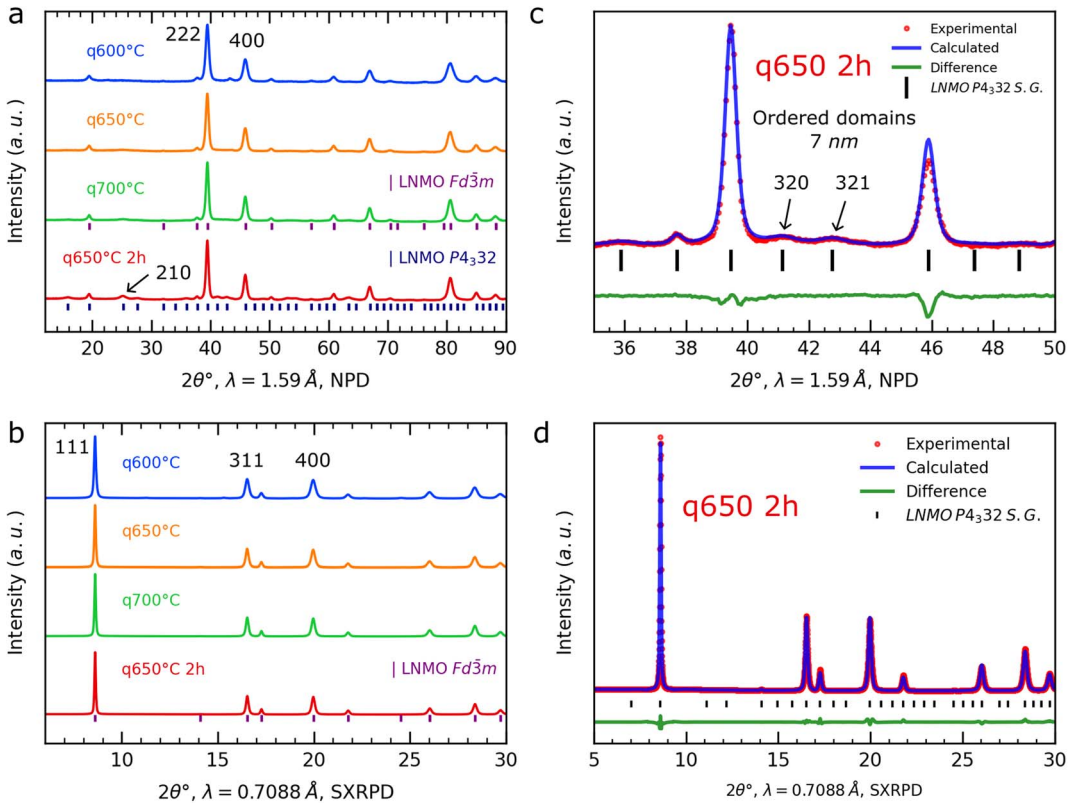

Fig. 2 NPD (a) and SXRPD (b) patterns of the quenched samples prepared from the 1 : 4 molar mixture of Li_2CO_3 and $Ni_{0.23}Mn_{0.77}(OH)_2$ under air. Experimental points, as well as calculated and difference profiles obtained after the Rietveld refinement of the NPD (c) and SXRPD (d) patterns of the sample quenched after 2 hours at 650 °C. Selected $2\theta°$ range of the Rietveld plot of NPD data is chosen to demonstrate the fitting of the superstructure reflections of the ordered LNMO phase.

refinement of the structure from the NPD pattern collected at T = 800 °C with the same two-phase model, as for SXRPD, provides reliable descriptions (Fig. S3b†).

To summarize this section, our *in situ* SXRPD and NPD study demonstrates that during the first stage of the solid-state synthesis of LNMO at $T \leq 700$ °C, the disordered Li-deficient LNMO spinel phase initially forms with Ni atoms occupying the Li sites. This off-stoichiometry in the LNMO phase is attributed to the incomplete chemical reaction between Li_2CO_3 the $Ni_xMn_{2-x}O_3$ transition metal oxide and $Ni_yMn_{1-y}O(OH)$ oxyhydroxide, which are formed after the dehydration of $Ni_{0.23}Mn_{0.77}(OH)_2$ hydroxide at $T \approx 300$ °C. The presence of amorphous and/or poorly crystalline phases next to the Li-deficient LNMO spinel phase is anticipated at this stage of synthesis. However, during the annealing of the LNMO sample at $T < 700$ °C, the ordered LNMO spinel phase forms, indicating that the ordered phase is thermodynamically stable at $T < 700$ °C.

At $T > 700$ °C, the oxygen release starts, leading to the formation of impurity phases. In the temperature range of 700–850 °C, a layered oxide impurity is formed, transformed to a rock salt impurity at $T > 850$ °C. The driving force for the phase transition from the layered oxide to rock salt impurity remains unclear but is most likely nested in compositional changes upon heating, as it is well-known that layered oxides typically possess a Li/M ratio close to one,[17,18] much higher than that observed in rock salt oxides. Unfortunately, the low crystallinity of the LNMO spinel and of the impurity phases, formed during heating of the mixture of Li_2CO_3 and $Ni_{0.23}Mn_{0.77}(OH)_2$,

Table 1 Lattice parameters, and Li/Ni and Mn/Ni ratios at the tetrahedral and octahedral sites respectively, compared for the quenched samples prepared under air from the mixture of Li_2CO_3 and $Ni_{0.23}Mn_{0.77}(OH)_2$. Results obtained from the combined Rietveld refinement of SXRPD and NPD data

Sample ID	Model	a, Å	Li/Ni, tetrahedra	Mn/Ni, octahedra
q600 °C	Disordered	8.1778(3)	0.956/0.044(1)	1.56/0.44(1)
q650 °C	Disordered	8.1781(2)	0.960/0.040(1)	1.55/0.45(1)
q700 °C	Disordered	8.1765(4)	0.981/0.019(2)	1.57/0.43(1)
q650 °C 2 h	Ordered	8.1746(2)	0.985/0.015(1)	1.54/0.46(2)

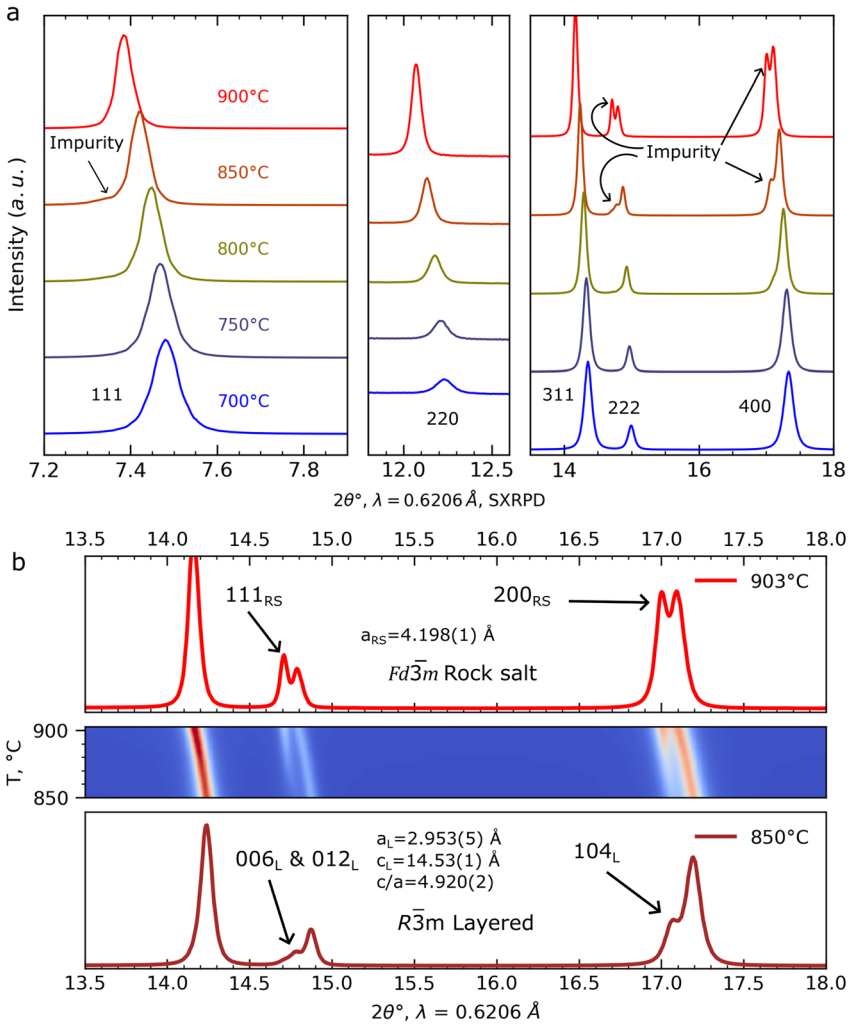

Fig. 3 Selected 2θ ranges of *in situ* SXRPD patterns collected for the 1 : 4 molar mixture of Li_2CO_3 and $Ni_{0.23}Mn_{0.77}(OH)_2$ at given temperatures (a). Contour plot representing evolution of the SXRPD patterns from 850 °C to 903 °C during the *in situ* experiment (b).

prevents us from determining the composition of the impurity phase.

Structural changes in LNMO spinel and impurity phases upon annealing

To improve angular resolution and simplify structural analysis, *in situ* temperature-controlled SXRPD experiments were performed on the highly crystalline as-prepared LNMO sample. These *in situ* experiments were performed under both air and oxygen atmospheres to study the impact of partial oxygen pressure on the phase equilibrium. As described in details in the experimental section, this LNMO sample with Mn/Ni = 77/23 ($LiNi_{0.46}Mn_{1.54}O_4$) was prepared from the thermal treatment of a 1 : 4 molar mixture of Li_2CO_3 and $Ni_{0.23}Mn_{0.77}(OH)_2$ at T = 1050 °C under a synthetic air atmosphere. The Rietveld analysis is given in details in supplementary information in Fig. S4† and reveals that small amounts of rock salt and layered oxides as impurities are present next to the spinel phase.

Similar phase transformations of the LNMO sample were observed for both atmospheres, air and oxygen, during the heating, and they appeared similar to those observed for the *in situ* SXRPD experiment performed starting from the 1 : 4 molar mixture of Li_2CO_3 and $Ni_{0.23}Mn_{0.77}(OH)_2$. Selected SXRPD patterns collected *in situ* upon heating the LNMO sample at given temperatures can be found in Fig. S5.† From T = 750 °C, the intensity of the reflections associated to the layered oxide impurity increases, as well as the intensity of the 220 reflection of the LNMO phase, showing for that latter an increasing amount of transition metal ions in the Li sites of the spinel structure. Finally, an extended annealing of the sample at 900 °C, in air or in oxygen, causes the phase transformation of the layered oxide impurity to the rock salt impurity (Fig. S6†). A detailed description of the model used for the sequential Rietveld refinement from this data set can be found in ESI,† with the LNMO spinel phase described by the general formula $(Li_{1-x}Ni_x)_{8a}(Ni_{0.46}Mn_{1.54})_{16d}O_4$. The results obtained are detailed in Fig. 5.

The lattice parameter of the LNMO phase is highly dependent on its composition and on the oxidation states of the Mn atoms. According to the Rietveld refinement from the NPD

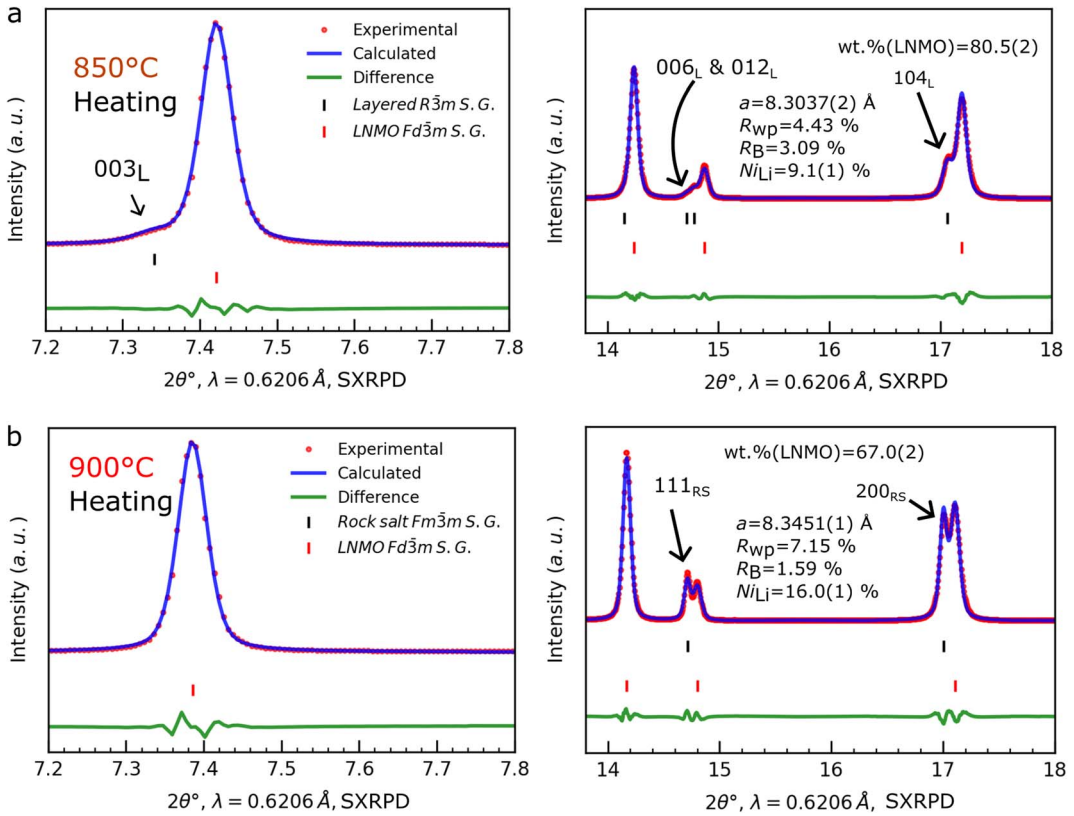

Fig. 4 Experimental points, as well as calculated and difference profiles obtained after the Rietveld refinement of the SXRPD patterns collected *in situ* for the 1 : 4 molar mixture of Li_2CO_3 and $Ni_{0.23}Mn_{0.77}(OH)_2$: at 850 °C (a) and at 900 °C (b). 2θ ranges are selected to highlight reflections of the layered oxide and rock salt impurities, respectively.

pattern of the pristine LNMO sample, the LNMO spinel phase has a chemical composition of $LiNi_{0.41(1)}Mn_{1.59(1)}O_4$ *i.e.* $LiNi_{0.41(1)}{}^{2+}Mn_{0.18(1)}{}^{3+}Mn_{1.41(1)}{}^{4+}O_4$. Upon heating of this pristine spinel sample, oxygen release starts at $T \approx 700$ °C, leading to the formation of the impurity phase and to the reduction of the Mn^{4+} cations to Mn^{3+}. Moreover, according to Cabana *et al.*,[5] the impurity phase has a Ni-enriched composition. As a result, the formation of the impurity phase increases the Mn content in the spinel (and consequently the amount of Mn^{3+} cations) which in turn increases its lattice parameters.

An increase in the slope of the lattice parameter change of the LNMO spinel phase with temperature (Fig. 5a) indicates an increase of Mn content. Smaller values of the lattice parameter of the LNMO phase under oxygen can be explained by lower Mn content in the LNMO phase and higher Li content at the 8*a* (Li) sites (Fig. 5c). It should be noted that a decrease in Li content in the LNMO phase results in additional reduction of Mn^{4+} to Mn^{3+} cations. The higher weight fractions of LNMO (Fig. 5b) and Li content in the LNMO phase (Fig. 5c) at a given temperature under oxygen atmosphere, compared to air, can be attributed to the higher partial oxygen pressure, which shifts the equilibrium towards the formation of the LNMO phase.

In the following, changes in the impurity phase will be discussed. The structural relationships between the layered oxide and rock salt are thoroughly discussed in ESI.† The refined lattice parameters a_L and c_L of the layered oxide impurity, along with the calculated c_L/a_L ratio, are given in Fig. 5d–f as a function of the temperature, while the refined M and Li contents at the 3*a* and 3*b* sites, as well as the overall Li content in the layered oxide phase, are shown in Fig. 5g–i. A sharp increase in the a_L is observed from $T \approx 825$ °C (Fig. 5d), whereas the c_L rises up to $T \approx 870$ °C before decreasing (Fig. 5e). The c_L/a_L ratio increases up to $T \approx 820$–830 °C (Fig. 5f), and then decreases until $T = 900$ °C. This evolution suggests an initial increase in the degree of ordering between Li and the transition metals M in the crystal structure of the layered phase at lower temperatures, followed by a decrease in ordering at higher temperatures. In the range of 750–800 °C, there is a rise in Li content at the 3*b* site (Fig. 5h) and in the overall Li content in the layered oxide phase (Fig. 5i). However, both parameters decrease at $T >$ 800 °C, supporting also a higher disorder of Li and M between the 3*a* and 3*b* sites (Fig. 5g and h) and a decrease in the c_L/a_L ratio (Fig. 5f). The chemical formula $(Li_{1-x-y}M_{x+y})_{3b}(Li_yM_{1-y})_{3a}O_2$ with $x > 0$ describes well the disordered layered oxide impurity phase.

During annealing at 900 °C under both atmospheres, this disordered layered oxide transforms to the rock salt phase as highlighted by the merging of the (006) and (012) diffraction peaks in the $R\bar{3}m$ S.G. into a single (111) peak in the $Fm\bar{3}m$ S.G. (Fig. S6†) and by the decrease of the c_L/a_L ratio from 4.95 to 4.90. The Rietveld refinement of the SXRPD patterns collected during heating at 900 °C (Fig. 6a) and after 5 hours of annealing under

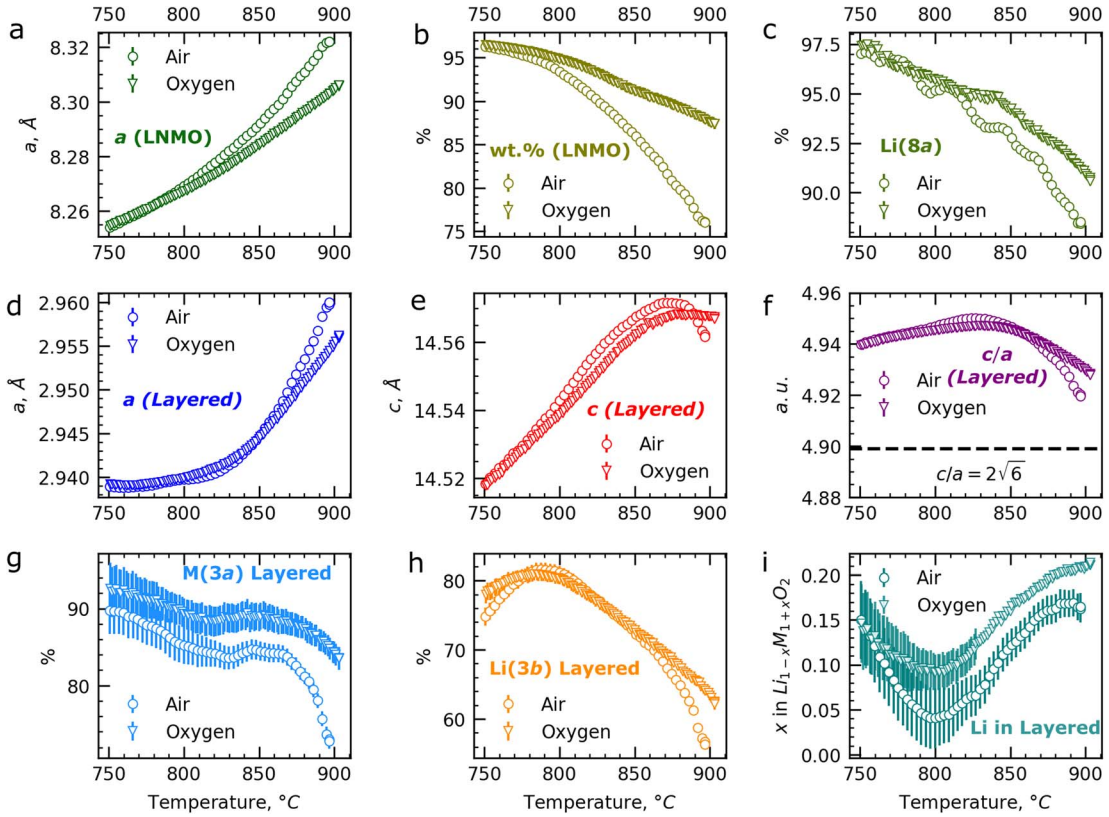

Fig. 5 Results obtained from the sequential Rietveld refinements of SXRPD patterns collected for the LNMO sample, in the range of 750–900 °C, under air and oxygen atmospheres. (a) Evolution of the lattice parameter, (b) weight fraction of the LNMO phase, (c) Li content at the 8*a* sites of the spinel structure, (d)–(f) lattice parameters and *c*/*a* ratio of the layered oxide phase, (g) transition metal (M) content at the 3*a*, M sites of the layered structure, (h) Li content at the 3*b*, Li sites of the layered structure, and (i) overall Li content in the layered oxide phase. On some graphs, the error bars are smaller than symbol size of data points.

air at this temperature (Fig. 6b) reveals a decrease in the Li content in the impurity phase: $Li_{0.84(1)}M_{1.16(1)}O_2$ for the first at 900 °C and $Li_{0.77(1)}M_{1.23(1)}O_2$ for the second after being maintained at 900 °C during 5 h. This further confirms that the Li content in the impurity phase controls the phase transition from the rhombohedral layered structure to the cubic rock salt structure.

Additionally, changes in the lattice parameter and weight fraction of the LNMO spinel phase, along with the Li content at the 8*a* site in its crystal structure, are also observed (Fig. 6). These structural changes in both phases during annealing also indicates that equilibrium states during heating were not fully achieved. Moreover, a pronounced asymmetry in the reflections of LNMO spinel and the impurity phase is observed at high 2θ angles, which can be attributed to strain broadening due to not homogeneous chemical composition of the phases in the sample.

To summarize this section, the following equation (eqn (2)) is proposed to describe the phase equilibrium during the synthesis in the temperature range of 750–900 °C:

$$LiM_2O_4 = p(Li_{1-x}M_x)M_2O_4 + qLi_{1-y}M_{1+y}O_2 + zO_2\uparrow \quad (2)$$

where M = Ni, Mn. The *p*, *q* and *z* coefficients can be calculated from the weight balance equation, if the exact compositions of LNMO and impurity phases were known. During high-temperature synthesis, the crystal structure of LNMO becomes Li-deficient due to the formation of the Li-enriched impurities. The crystal structure of the impurity undergoes the transformation from the rhombohedral layered to the cubic rock salt oxides at $T \geq 900$ °C. Due to limiting temperature of the used hot air blower, the described *in situ* SXRPD experiment with the LNMO sample was performed only up to $T = 900$ °C. Considering the similar scattering of Ni and Mn atoms, the exact composition of the LNMO phase remains unclear. Therefore, a series of samples quenched from $T = 750$–950 °C under air was prepared to study the phase equilibrium at $T > 900$ °C and to combine SXRPD and NPD diffraction for better insights into the composition of the LNMO phase.

Evolution of the composition of the LNMO spinel phase

Selected 2θ ranges of the SXRPD patterns of samples quenched under air from 750 °C, 800 °C, 850 °C, 900 °C, and 950 °C (noted as q750 °C–q950 °C) are shown in Fig. S7.† The same increase, with temperature, of the intensity of the (220) reflection of the LNMO spinel phase was observed, indicating that transition metal cations are occupying the Li sites. However, the

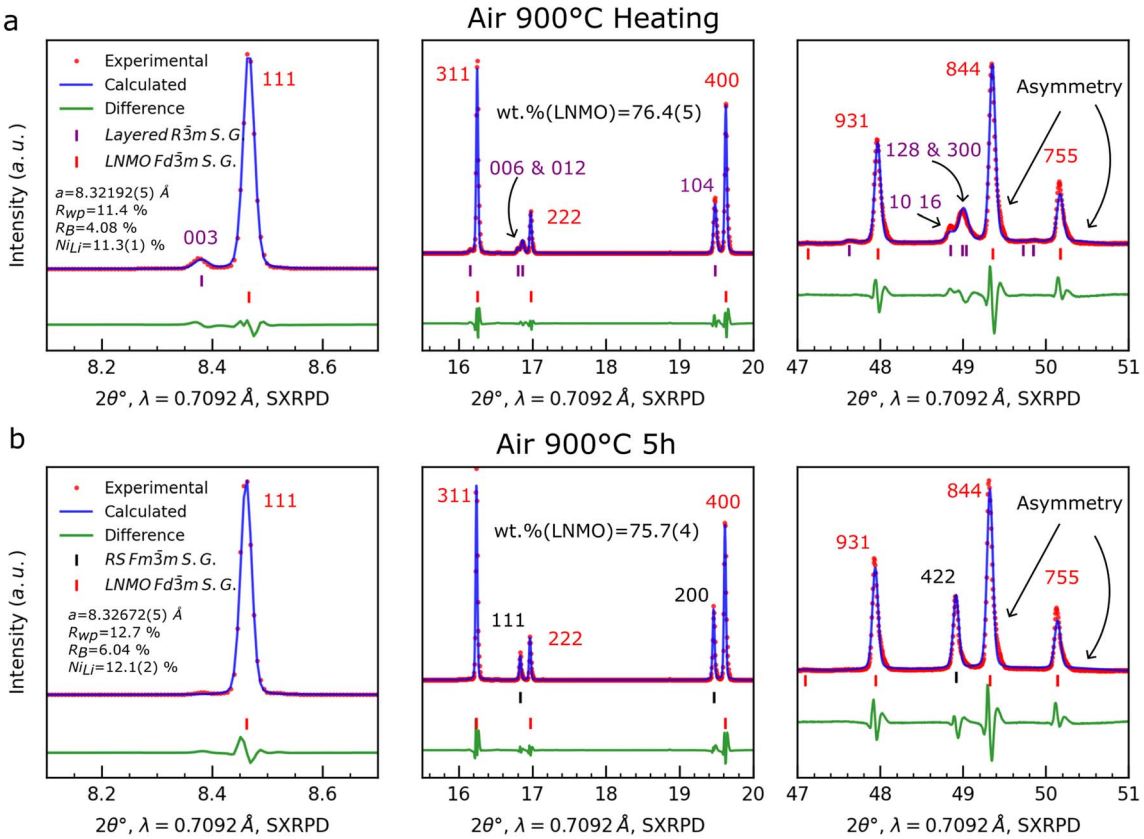

Fig. 6 Experimental points, as well as calculated and difference profiles after the Rietveld refinements of SXRPD patterns for the LNMO samples: collected at 900 °C during heating (a) and after 5 h of annealing at 900 °C (b).

crystallinity of these samples declines with an increase of the temperature, making the observed reflections broader. This deterioration of the crystallinity is likely attributed to the inhomogeneity of the composition at the particle level, caused by the quenching procedure.

The detailed procedure of the Rietveld refinements from SXRPD and NPD data of the LNMO samples, quenched from $T =$ 750–900 °C, can be found in ESI.† It should be noted that due to the bad crystallinity of the q950 °C sample and the possible overlapping of the reflections of the LNMO and impurity phases in the SXRPD and NPD patterns, the Rietveld refinements for the q950 °C sample were not performed, using the same model, as for the q750 °C–q900 °C. The Rietveld refinement of the q950 °C is described below.

Combining SXRPD and NPD allows us to clarify the cationic composition at the tetrahedral 8*a* and octahedral 16*d* sites in the crystal structure of the LNMO spinel phase. For this purpose, the following structural model was proposed: $(Li_cNi_{1-y-c}Mn_y)_{8a}(Ni_{0.5-z}Mn_{1.5+z})_{16d}O_4$. From the Rietveld refinement of the SXRPD data, the *c* parameter, representing the Li content at the 8*a* sites, is determined. Subsequently, the Rietveld refinement of the NPD data allows for the refinement of the *y* and *z* values, and thus of the occupancy factors of both Mn and Ni at the 8*a* and 16*d* sites. Results obtained after the Rietveld refinement of the SXRPD and NPD data are gathered in Fig. 7. The experimental points, as well as calculated and difference plots after the Rietveld refinements can be found in Fig. S8–S11.†

An increase of the lattice parameter of the LNMO spinel phase (Fig. 7a) indicates a change of its composition and as previously discussed, this increase can be attributed to the higher amount of Mn^{3+} cations in the structure. Additionally, due to the oxygen release at $T \geq 700$ °C under air, the impurity phase forms (Fig. 7b), leading to Li loss from the LNMO phase and to the occupation of the 8*a* sites by Ni and/or Mn atoms, as shown in the previous section. Surprisingly, the combination of SXRPD and NPD data shows that both Ni and Mn atoms occupy the 8*a* sites (Fig. 7c). Furthermore, as the temperature increases, more Mn atoms are found at this site, as well as at the 16*d* sites (Fig. 7d), leading to a Mn-rich and Li-deficient composition for LNMO.

The increase of the average interatomic distance *d*(M–O) at the 16*d* site (Fig. 7c) corresponds to the increase of the Mn content at this site. An increase of the average interatomic distance *d*(M–O) at the 8*a* site is also observed suggested that Mn^{2+} and Ni^{2+} cations occupy the 8*a* sites. Indeed, the Mn^{2+} cations possess a larger ionic radius of 0.66 Å (CN = 4) *versus* Li^+ (0.59 Å) and Ni^{2+} (0.55 Å) cations, and even more *versus* Mn^{4+} (0.39 Å). Therefore, the increase of the *d*(M–O) at the 8*a* sites aligns only with the increase of amount of Mn^{2+} cations at the 8*a* sites.

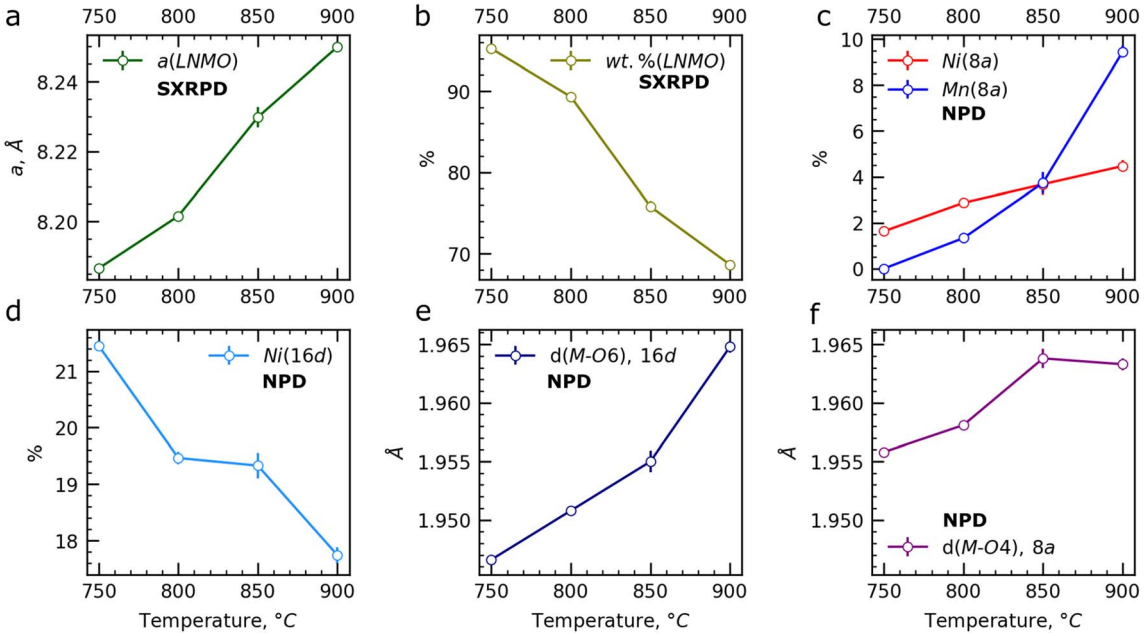

Fig. 7 Lattice parameter (a), weight fraction (b), Ni and Mn content at the Li 8*a* sites (c), Ni content at the M 16*d* sites, the Mn content being the complement of Ni in the 16*d* sites (d), interatomic distances at the 16*d* (e) and 8*a* (f) sites in the LNMO spinel phase after the Rietveld refinement of the SXRPD and NPD patterns of the q750 °C, q800 °C, q850 °C and q900 °C samples. The data source of each refined parameter is indicated in bold on the corresponding graph.

It should be noted that Chen *et al.*,[11] using the Rietveld refinement of data collected during *in situ* NPD under an Ar atmosphere, suggested the occupation of the 8*a* sites by Mn and Ni atoms. Our combined SXRPD and NPD study of the quenched samples of LNMO confirms this suggestion and allows to propose the chemical compositions of the LNMO phase in these samples (Table 2). As seen in Table 2, the average oxidation state of Mn cations decreases with increasing temperature. However, the average oxidation state of +3.64 for Mn in the q900 °C sample does not clearly indicate the presence of Mn^{2+} cations. The formation of Mn^{2+} cations could be explained by the disproportionation reaction: $2Mn^{3+} \rightarrow Mn^{2+} + Mn^{4+}$. It can be assumed that Mn^{2+} cations occupy at the 8*a* sites in the crystal structure of the LNMO spinel phase. However, it is difficult to determine definitively where the Mn^{4+} cations are. One possibility could be into the impurity phase as it will be supported in the next section.

Table 2 Chemical compositions and average oxidation states of Mn calculated in the quenched samples from the results of the Rietveld refinement of SXRPD and NPD data, using the structural model $(Li_cNi_{1-y-c}Mn_y)_{8a}(Ni_{0.5-z}Mn_{1.5+z})_{16d}O_4$, where *c* is the Li content at the 8*a* site, derived from the Rietveld refinement of SXRPD data and fixed in the refinement of NPD data, and *y* and *z* are refined parameters in the Rietveld refinement of NPD data

Sample	Composition of the LNMO phase	Mn average oxidation state
q750 °C	$Li_{0.984(1)}Ni_{0.445(3)}Mn_{1.571(2)}O_4$	3.90
q800 °C	$Li_{0.958(4)}Ni_{0.418(6)}Mn_{1.624(6)}O_4$	3.82
q850 °C	$Li_{0.926(6)}Ni_{0.42(1)}Mn_{1.65(1)}O_4$	3.77
q900 °C	$Li_{0.861(4)}Ni_{0.40(1)}Mn_{1.74(1)}O_4$	3.64

Formation of the Li-rich layered oxide impurity at $T \geq 900$ °C

On the SXRPD pattern of the q950 °C sample, new unknown reflections are observed, that we attributed (Fig. 8) to a Li-rich layered oxide with cell parameters $a = 2.857(1)$ Å, $c = 14.34(1)$ Å ($R\bar{3}m$ S.G.). Indeed, as typically observed for Li-rich layered oxides, main reflections can be indexed in the $R\bar{3}m$ S.G., whereas low-intense, broad and asymmetric (diffuse) superstructure reflections, coming from faults in the stacking of the layers containing ordered Li and transition metal cations, can be described only in the monoclinic *C*2/*m* S.G.[19,20]

To confirm further the presence of the Li-rich layered oxide phase, a Raman spectroscopy study of the quenched samples was also carried out in comparison with $Li_{1.2}Ni_{0.2}Mn_{0.6}O_2$ (Fig. 9a). Indeed, Raman spectroscopy was proven to be an efficient tool to probe various types of atomic ordering for both layered and spinel oxides.[16,21] The spectra of the q750, q800 and q900 °C samples correspond to that of the pristine disordered LNMO sample. The band at 635 cm^{-1} is associated with the stretching of the Li–O bond, where the oxygen is primarily bonded to Mn atoms, enabling the monitoring of the Mn oxidation state.[22] This band shifts to lower energies for samples resulting from higher quenching temperatures, as a result of bigger amounts of Mn^{4+} cations reduced into Mn^{3+} cations. This is also in good agreement with an increasing intensity of the shoulder observed at $\approx$655 cm^{-1}, which is attributed to the Jahn–Teller distortion of the $Mn^{3+}O_6$ octahedra. The band at 495 cm^{-1} corresponds to the Li–O bond stretching, with in this

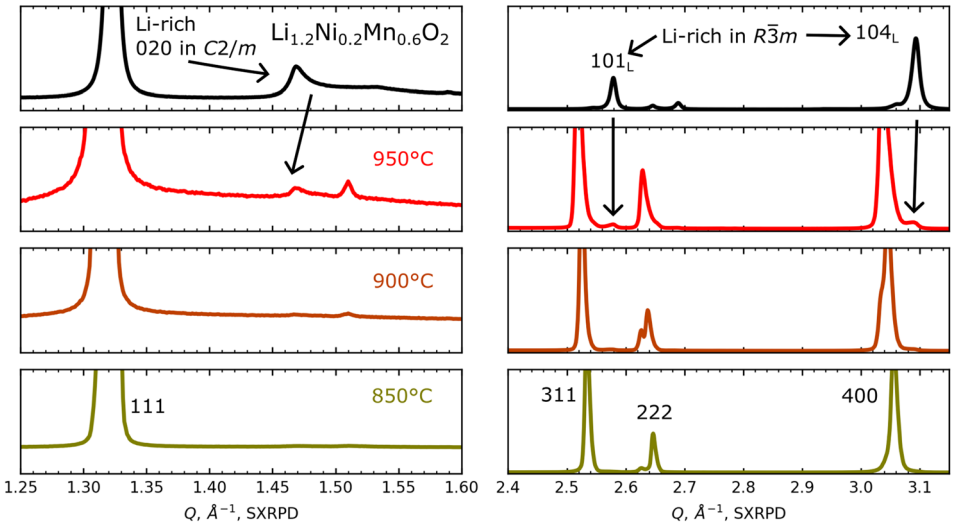

Fig. 8 Comparison of the SXRPD pattern of the Li-rich $Li_{1.2}Ni_{0.2}Mn_{0.6}O_2$ oxide with the SXRPD patterns of the selected quenched samples. The ranges are chosen to highlight the superstructure reflections of the Li-rich layered oxide (left) and its main reflections (right).

case the oxygen predominantly bonded to Ni atoms. The position of this band changes in parallel to that at 635 cm^{-1} with the partial substitution of Ni^{2+} by Mn^{3+} upon increasing temperature.

The q950 °C sample is significantly different from the others in the range of 250–450 cm^{-1} and a comparison with that of $Li_{1.2}Ni_{0.2}Mn_{0.6}O_2$ shows that the bands observed in this range can be assigned to the Li-rich layered oxide phase whose presence was also confirmed by SXRPD.

Additionally, the Raman data suggest an inhomogeneous distribution of phases in both the q900 °C and q950 °C samples (Fig. 9b). In the q950 °C sample, spectra collected from different particles correspond either to the LNMO spinel phase or to the Li-rich layered oxide phase. Similarly, in the q900 °C sample,

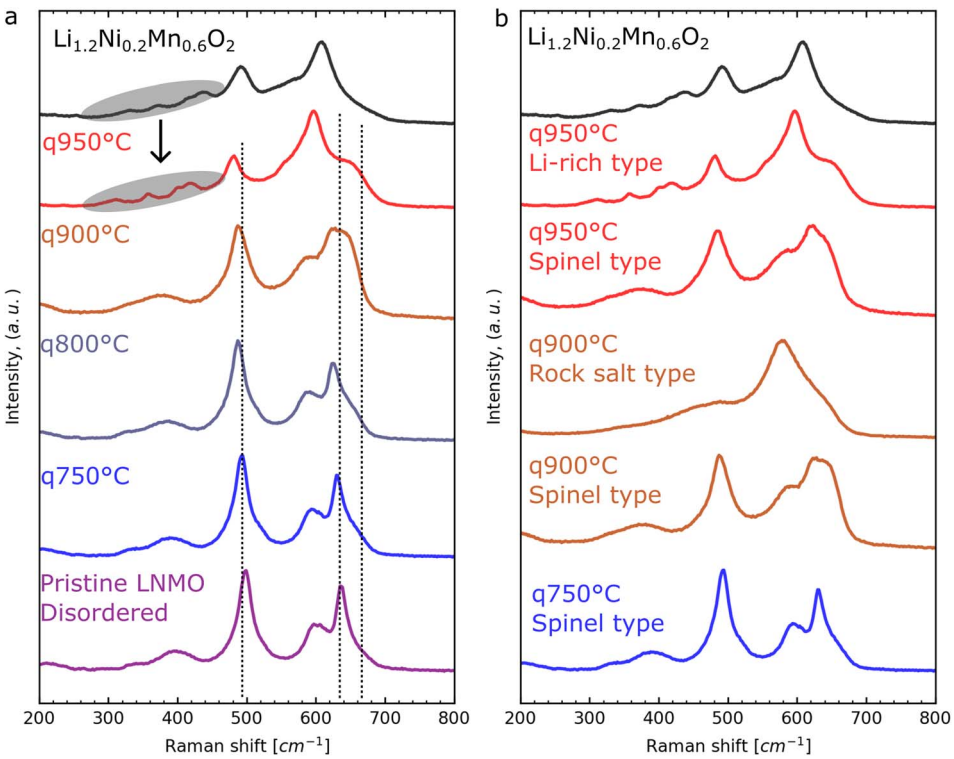

Fig. 9 Comparison of selected Raman spectra of the pristine LNMO, quenched LNMO and $Li_{1.2}Ni_{0.2}Mn_{0.6}O_2$ samples (a). Comparison of the different Raman spectra that can be obtained for the q900 °C and q950 °C samples, collected from different particles, with the spectra of the q750 °C and $Li_{1.2}Ni_{0.2}Mn_{0.6}O_2$ samples (b).

spectra from different particles align with those of the rock salt phase.

To investigate distribution of the impurity phases at the particle level in the q950 °C sample, electron diffraction (ED) patterns were collected at two different points of the single crystal (Fig. 10). One of the ED patterns can be indexed in the $Fd\bar{3}m$ S.G., corresponding to the LNMO spinel phase (orange zone). The two other ED patterns collected from the second point (white zone) cannot be described by the $Fd\bar{3}m$ S.G. The first can be fully indexed in the $R\bar{3}m$ S.G. in the zone axis $[14\ 7\ 1]_R$, whereas the second, obtained from the first tilting the sample holder of ≈13.3°, changes the zone axis to $[8\ 4\ 1]_R$ and shows main spots that can still be indexed in in the $R\bar{3}m$ S.G. and additional lower-intensity spots that can be indexed into the $C2/m$ space group. Those latter are attributed to the cationic ordering within the transition metal layer and the associated diffusive scattering lines to the stacking faults, typical as already reported to Li-rich layered oxides.[23–26]

Based on SXRPD, Raman spectroscopy and ED data, it can then be concluded that the Li-rich layered oxide impurity phase forms at $T \geq 900$ °C. However, the question remains as how many impurity phases are present in the sample at $T \geq 900$ °C. As noted earlier, due to the poor crystallinity of the q950 °C sample, if reflections from the rock salt phase are present, they overlap with the reflections of the LNMO spinel phase. Additionally, the Raman data suggest an inhomogeneous distribution of phases in both the q900 °C and q950 °C samples (Fig. 9b). In the q950 °C sample, spectra collected from different particles correspond either to the LNMO spinel phase or to the Li-rich layered oxide phase. Similarly, in the q900 °C sample, spectra from different particles align with those of the rock salt phase. However, it is important to note that the Raman spectra of layered oxides and rock salts appear similar (Fig. S12†), making it difficult to distinguish between these two phases using Raman spectroscopy alone.

To confirm further the presence of the rock salt phase, Rietveld refinements (see details in ESI†) were performed from the SXRPD pattern of the q950 °C sample using both a three-phase model (LNMO spinel, rock salt, and Li-rich layered oxide phases) and a two-phase model (LNMO spinel and Li rich layered oxide phases). The experimental points, calculated profiles, and difference profiles are shown in Fig. S13.† As it can be seen, the three-phase model provides a better fit of the SXRPD pattern: twice lower R_B factor and lower G.O.F. This suggests that during the synthesis of LNMO at $T \geq 900$ °C, the sample contains three coexisting phases: LNMO spinel, rock salt, and Li-rich layered oxide.

It is worth noting a certain similarity in phase transformations during synthesis in both LNMO and $LiMn_2O_4$ spinel systems. In studies by Thackeray *et al.*,[27] Tarascon *et al.*,[28] and Yamada *et al.*,[29] it was shown that during the synthesis of $LiMn_2O_4$ at temperatures above the onset of oxygen loss, a Li-rich layered oxide Li_2MnO_3 impurity phase also forms. However, the spinel phase undergoes a phase transition from a cubic to a tetragonal structure. The formation of the rock salt phase does not occur. Therefore, it can be assumed that the LNMO spinel phase at high temperatures begins to behave similarly to the $LiMn_2O_4$ phase, which may be related to the increased Mn content in the LNMO spinel phase. However, in the case of LNMO, the spinel phase does not undergo a phase transition to a tetragonal structure. Yamada *et al.*[29] suggested that the transition from cubic to tetragonal occurs when the

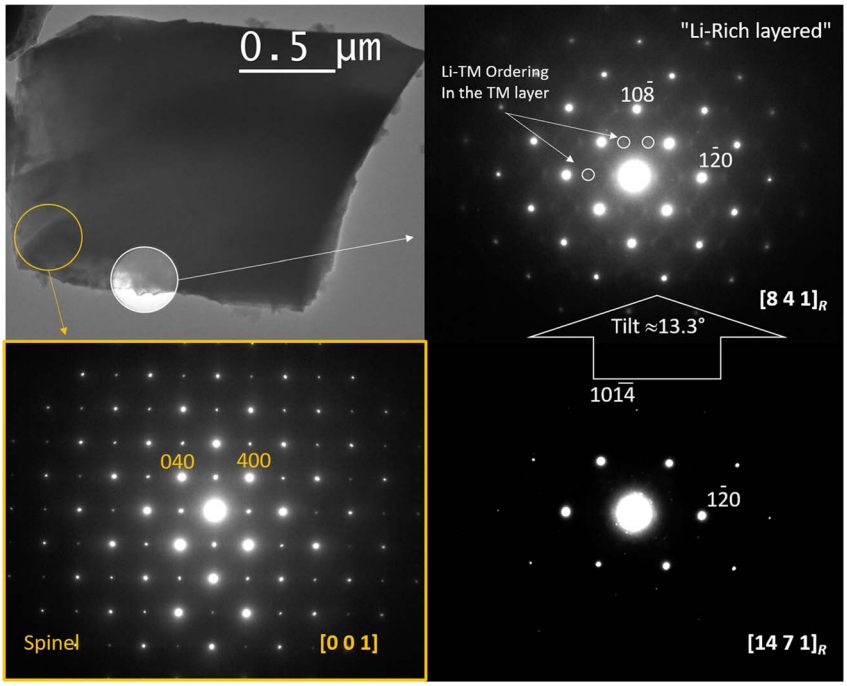

Fig. 10 TEM image of the single crystal in the q950 °C sample and the corresponding electron diffraction patterns collected at different points of this crystal.

oxidation state of Mn cations is less than 3.5. According to our results, the average oxidation state of Mn in the LNMO spinel phase in the q900 °C sample is 3.64. It can be assumed that at higher temperatures, when the average oxidation state of Mn in the LNMO spinel phase drops below 3.5, a transition to the tetragonal phase may occur.

Conclusions

In this study, we employed SXRPD and NPD to investigate phase equilibria during the synthesis of LNMO spinel materials. The LNMO phase begins to form at $T \approx 460$ °C during the annealing of the 1 : 4 molar mixture of Li_2CO_3 and $Ni_{0.23}Mn_{0.77}(OH)_2$. By $T \approx 700$ °C, only the LNMO phase is observed in the SXRPD and NPD patterns. However, Rietveld refinements of the data reveal that the resulting LNMO phase is Li-deficient, with a small amount of Ni^{2+} cations occupying the tetrahedral Li (8*a*) sites. This non-stoichiometry is attributed to the incomplete chemical reaction at this stage of synthesis, along with the presence of amorphous and/or poorly crystallized phases. At $T > 700$ °C, oxygen release occurs from the LNMO sample, leading to the formation of an impurity phase. In the temperature range of 750–900 °C, a layered oxide impurity phase is present in the sample.

The Rietveld refinement results from both the *in situ* SXRPD experiments and the series of quenched samples show that during synthesis the composition of the LNMO phase significantly deviates from the target composition, with an excess of Mn and a deficiency of Li. By combining SXRPD and NPD to study the series of quenched samples, we established that as Li is lost from the LNMO spinel phase, Ni and Mn atoms begin to occupy the 8*a* Li sites, with Mn atoms increasingly occupying these sites as the temperature rises. An analysis of the average M–O bond distances suggests that these atoms exist as divalent Ni^{2+} and Mn^{2+} cations. The formation of Mn^{2+} cations could be explained by the disproportionation reaction $2Mn^{3+} \rightarrow Mn^{2+} + Mn^{4+}$. The results of SXRPD, Raman spectroscopy, and electron diffraction indicate that at $T \geq 900$ °C a Li-rich layered oxide impurity phase forms alongside the rock salt impurity, causing the coexistence of three phases during the high-temperature synthesis of LNMO. These findings significantly enhance our understanding of the phase and structural transformations during synthesis and underscore the exceptional complexity of the LNMO system. We believe this work will serve as an excellent guide for the synthesis of LNMO positive electrode materials for LIBs.

Data availability

We certify that the data corresponding to the results reported in our paper "Phase equilibrium during the synthesis of $LiNi_{0.46}Mn_{1.54}O_4$: comprehensive X-ray & neutron powder diffraction study" by Tertov *et al.* will be available when asked, those mentioned in the manuscript but also in ESI.†

Conflicts of interest

There are no conflicts to declar.

Acknowledgements

The authors thank Emmanuel Petit, Cathy Denage, Jacob Olchowka, Jérôme Kalisky and Eric Lebraud from ICMCB, Alain Daramsy and Ludovic Gendrin from ILL, and Alexander Missyul from ALBA for their technical support. The authors thank also Jazer J. Togonon for his support in the collection and discussion of the all data on Li-rich layered oxides. The authors acknowledge ILL (Grenoble, France) for neutron powder diffraction experiments on the D20 beamline (**https://doi.org/10.5291/ILL-DATA.5-24-692**) and D2B beamline (**https://doi.org/10.5291/ILL-DATA.5-24-691**), ALBA (Barcelona, Spain) for synchrotron X-ray powder diffraction experiments on the MSPD beamline (proposal 2022097144). They thank the European Union's Horizon 2020 research and InnovaXN programme under the Marie Skłodowska-Curie grant agreement no. 847439 and ILL for the funding of I. Tertov PhD thesis, as well as Umicore, the Région Nouvelle Aquitaine and the French National Research Agency (STORE-EX Labex Project ANR-10-LABX-76-01) for the financial support of their research.

References

1 G. Liang, V. K. Peterson, K. W. See, Z. Guo and W. K. Pang, Developing high-voltage spinel $LiNi_{0.5}Mn_{1.5}O_4$ cathodes for high-energy-density lithium-ion batteries: current achievements and future prospects, *J. Mater. Chem. A*, 2020, **8**, 15373–15398, DOI: **10.1039/D0TA02812F**.

2 J.-H. Kim, A. Huq, M. Chi, N. P. W. Pieczonka, E. Lee, C. A. Bridges, M. M. Tessema, A. Manthiram, K. A. Persson and B. R. Powell, Integrated Nano-Domains of Disordered and Ordered Spinel Phases in $LiNi_{0.5}Mn_{1.5}O_4$ for Li-Ion Batteries, *Chem. Mater.*, 2014, **26**, 4377–4386, DOI: **10.1021/cm501203r**.

3 D. Pasero, N. Reeves, V. Pralong and A. R. West, Oxygen Nonstoichiometry and Phase Transitions in $LiMn_{1.5}Ni_{0.5}O_{4-\delta}$, *J. Electrochem. Soc.*, 2008, **155**, A282, DOI: **10.1149/1.2832650**.

4 L. Cai, Z. Liu, K. An and C. Liang, Unraveling structural evolution of $LiNi_{0.5}Mn_{1.5}O_4$ by in situ neutron diffraction, *J. Mater. Chem. A*, 2013, **1**, 6908, DOI: **10.1039/c3ta00145h**.

5 J. Cabana, M. Casas-Cabanas, F. O. Omenya, N. A. Chernova, D. Zeng, M. S. Whittingham and C. P. Grey, Composition-Structure Relationships in the Li-Ion Battery Electrode Material $LiNi_{0.5}Mn_{1.5}O_4$, *Chem. Mater.*, 2012, **24**, 2952–2964, DOI: **10.1021/cm301148d**.

6 M. Casas-Cabanas, C. Kim, J. Rodríguez-Carvajal and J. Cabana, Atomic defects during ordering transitions in $LiNi_{0.5}Mn_{1.5}O_4$ and their relationship with electrochemical properties, *J. Mater. Chem. A*, 2016, **4**, 8255–8262, DOI: **10.1039/C6TA00424E**.

7 L. Wang, H. Li, X. Huang and E. Baudrin, A comparative study of Fd-3m and P4332 "$LiNi_{0.5}Mn_{1.5}O_4$", *Solid State Ionics*, 2011, **193**, 32–38, DOI: 10.1016/j.ssi.2011.04.007.

8 H. Duncan, B. Hai, M. Leskes, C. P. Grey and G. Chen, Relationships between Mn^{3+} Content, Structural Ordering, Phase Transformation, and Kinetic Properties in $LiNi_xMn_{2-x}O_4$ Cathode Materials, *Chem. Mater.*, 2014, **26**, 5374–5382, DOI: 10.1021/cm502607v.

9 I. Tertov, H. Kwak, E. Suard, P.-E. Cabelguen, S. Kumakura, F. Fauth, T. Hansen, C. Masquelier and L. Croguennec, Impact of Mn/Ni and Li/(Mn+Ni) ratios on phase equilibrium and electrochemical performance of the high voltage spinel $LiNi_{0.5}Mn_{1.5}O_4$, *J. Power Sources*, 2024, **623**, 235447, DOI: 10.1016/j.jpowsour.2024.235447.

10 P. Stüble, V. Mereacre, H. Geßwein and J. R. Binder, On the Composition of $LiNi_{0.5}Mn_{1.5}O_4$ Cathode Active Materials, *Adv. Energy Mater.*, 2023, **13**, 2203778, DOI: 10.1002/aenm.202203778.

11 Y. Chen and K. An, Unraveling transition-metal-mediated stability of spinel oxide via in situ neutron scattering, *J. Energy Chem.*, 2022, **68**, 60–70, DOI: 10.1016/j.jechem.2021.10.024.

12 F. Fauth, R. Boer, F. Gil-Ortiz, C. Popescu, O. Vallcorba, I. Peral, D. Fullà, J. Benach and J. Juanhuix, The crystallography stations at the Alba synchrotron, *Eur. Phys. J. Plus*, 2015, **130**, 160, DOI: 10.1140/epjp/i2015-15160-y.

13 V. Petříček, M. Dušek and L. Palatinus, Crystallographic Computing System JANA2006: General features, *Zeitschrift für Kristallographie – Crystalline Materials*, 2014, **229**, 345–352, DOI: 10.1515/zkri-2014-1737.

14 J. Rodríguez-Carvajal, Recent advances in magnetic structure determination by neutron powder diffraction, *Phys. B*, 1993, **192**, 55–69, DOI: 10.1016/0921-4526(93)90108-I.

15 M. Casas-Cabanas, Atomic defects during ordering transitions in $LiNi_{0.5}Mn_{1.5}O_4$ and their relationship with electrochemical properties, *J. Mater. Chem. A*, 2016, **4**, 8255–8262, DOI: 10.1039/C6TA00424E.

16 G. Oney, J. Serrano-Sevillano, M. Ben-Yahia, J. Olchowka, E. Suard, F. Weill, A. Demortiere, M. Casas-Cabanas, L. Croguennec and D. Carlier, Identification of Degree of Ordering in Spinel $LiNi_{0.5}Mn_{1.5}O_4$ through NMR and Raman Spectroscopies Supported by Theoretical Calculations, *Energy Storage Mater.*, 2024, **70**, 103486.

17 E. McCalla and J. R. Dahn, The spinel and cubic rocksalt solid-solutions in the Li–Mn–Ni oxide pseudo-ternary system, *Solid State Ionics*, 2013, **242**, 1–9, DOI: 10.1016/j.ssi.2013.04.003.

18 M. Bianchini, M. Roca-Ayats, P. Hartmann, T. Brezesinski and J. Janek, There and Back Again—The Journey of $LiNiO_2$ as a Cathode Active Material, *Angew. Chem., Int. Ed.*, 2019, **58**, 10434–10458, DOI: 10.1002/anie.201812472.

19 S. Pajot, P. Feydi, F. Weill, M. Ménétrier, G. Yildirim, L. Simonin and L. Croguennec, Synthesis of Li and Mn-Rich Layered Oxides as Concentration-Gradients for Lithium-Ion Batteries, *J. Electrochem. Soc.*, 2018, **165**, A425–A433, DOI: 10.1149/2.0031803jes.

20 H. Koga, L. Croguennec, P. Mannessiez, M. Ménétrier, F. Weill, L. Bourgeois, M. Duttine, E. Suard and C. Delmas, $Li_{1.20}Mn_{0.54}Co_{0.13}Ni_{0.13}O_2$ with Different Particle Sizes as Attractive Positive Electrode Materials for Lithium-Ion Batteries: Insights into Their Structure, *J. Phys. Chem. C*, 2012, **116**, 13497–13506, DOI: 10.1021/jp301879x.

21 J. Hong, D.-H. Seo, S.-W. Kim, H. Gwon, S.-T. Oh and K. Kang, Structural evolution of layered $Li_{1.2}Ni_{0.2}Mn_{0.6}O_2$ upon electrochemical cycling in a Li rechargeable battery, *J. Mater. Chem.*, 2010, **20**, 10179–10186, DOI: 10.1039/c0jm01971b.

22 L. Boulet-Roblin, C. Villevieille, P. Borel, C. Tessier, P. Novák and M. Ben Yahia, Versatile Approach Combining Theoretical and Experimental Aspects of Raman Spectroscopy to Investigate Battery Materials: The Case of the $LiNi_{0.5}Mn_{1.5}O_4$ Spinel, *J. Phys. Chem. C*, 2016, **120**, 16377–16382, DOI: 10.1021/acs.jpcc.6b04155.

23 C. Genevois, H. Koga, L. Croguennec, M. Ménétrier, C. Delmas and F. Weill, Insight into the Atomic Structure of Cycled Lithium-Rich Layered Oxide $Li_{1.20}Mn_{0.54}Co_{0.13}Ni_{0.13}O_2$ Using HAADF STEM and Electron Nanodiffraction, *J. Phys. Chem. C*, 2015, **119**, 75–83, DOI: 10.1021/jp509388j.

24 A. Boulineau, L. Croguennec, C. Delmas and F. Weill, Reinvestigation of Li_2MnO_3 Structure: Electron Diffraction and High Resolution TEM, *Chem. Mater.*, 2009, **21**, 4216–4222, DOI: 10.1021/cm900998n.

25 A. Boulineau, L. Croguennec, C. Delmas and F. Weill, Structure of Li_2MnO_3 with different degrees of defects, *Solid State Ionics*, 2010, **180**, 1652–1659, DOI: 10.1016/j.ssi.2009.10.020.

26 J. G. Wen, J. Bareño, C. H. Lei, S. H. Kang, M. Balasubramanian, I. Petrov and D. P. Abraham, Analytical electron microscopy of $Li_{1.2}Co_{0.4}Mn_{0.4}O_2$ for lithium-ion batteries, *Solid State Ionics*, 2011, **182**, 98–107, DOI: 10.1016/j.ssi.2010.11.030.

27 M. M. Thackeray, M. F. Mansuetto and J. B. Bates, Structural stability of $LiMn_2O_4$ electrodes for lithium batteries, *J. Power Sources*, 1997, **68**, 153–158, DOI: 10.1016/S0378-7753(96)02624-9.

28 J. M. Tarascon, W. R. McKinnon, F. Coowar, T. N. Bowmer, G. Amatucci and D. Guyomard, Synthesis Conditions and Oxygen Stoichiometry Effects on Li Insertion into the Spinel $LiMn_2O_4$, *J. Electrochem. Soc.*, 1994, **141**, 1421–1431, DOI: 10.1149/1.2054941.

29 A. Yamada, K. Miura, K. Hinokuma and M. Tanaka, Synthesis and Structural Aspects of $LiMn_2O_{4\pm\delta}$ as a Cathode for Rechargeable Lithium Batteries, *J. Electrochem. Soc.*, 1995, **142**, 2149–2156, DOI: 10.1149/1.2044266.